JOURNAL OF PROPULSION AND POWER
Vol. 12, No. 1, January–February 1996

Computational Analysis of the Unsteady Type IV Shock Interaction of Blunt Body Flows

Charles A. Lind* and Mark J. Lewis†
University of Maryland, College Park, Maryland 20742

A thin-layer approximation to the two-dimensional Navier–Stokes equations, coupled with the total variation diminishing scheme, is used to examine a type IV shock interaction at Mach 8. The calculations reveal that the apparent unsteadiness of the type IV interaction is related to the formation and shedding of shear layers within the shock layer and acoustical feedback between the distorted bow shock and the body. A Fourier analysis of the flowfield indicates that this shedding frequency is the same frequency associated with the motion of the supersonic jet. The effects of shock impingement angle and shock strength on the location and magnitude of the peak pressure are also studied and it is shown that changes in the impinging shock angle can strongly affect the peak surface pressure and the supersonic jet position. Further examination of the unsteady behavior of the interaction reveals that a small change in the impinging shock angle can change the flowfield from steady to unsteady.

Nomenclature

A, B	=	grid-clustering parameters
D, H	=	grid-clustering parameters
l	=	reference length
M	=	Mach number
Pr	=	Prandtl number
p	=	pressure
Re	=	Reynolds number
r	=	cowl radius
T	=	temperature
t	=	time
u, v	=	x, y component of velocity
β	=	shock angle
γ	=	ratio of specific heats
$\Delta( )$	=	change in ( )
δ	=	shock standoff distance
θ	=	angular measurement
μ	=	viscosity
ξ, η	=	transformed coordinates

Subscripts

j	=	jet
s	=	shock
t	=	total
v	=	viscous
∞	=	freestream

Introduction

THE practicality of a hypersonic vehicle will depend on the design of a weight-saving, engine-integrated airframe, in which the forebody acts as the engine compression surface and the aftbody serves as the engine nozzle, as shown in Fig. 1. To properly design the inlet of such a vehicle, a detailed analysis of the flowfield is essential. Of particular importance is the interaction of the shock formed on the compression surface, the inlet shock, with the shock formed on the engine cowl, the cowl shock.

When the inlet shock interacts with the most forward part of the cowl bow shock, the result is a very complex flowfield with extremely high pressure and heat transfer rates in a very localized region. Experimental as well as computational results have shown that these pressure loads and intense heating rates can be up to 30 times larger than those of the noninterfering case.[1–6] In addition, this phenomenon is not limited to the engine cowl lip region, but may also be of concern on other areas of a transatmospheric vehicle, including the wing and tail sections[7] and at pylon couplings for multistage vehicles.

The type IV shock interaction, shown in Fig. 2, is one of six types of shock interactions first categorized by Edney.[1] In his work, Edney described the geometry of the six different flowfields, as determined by schlieren photographs, and also presented experimental measurements of the heat transfer rates and pressure loads for blunted bodies of different shapes.

It has been experimentally shown that for the type IV shock interaction, the peak pressure, heat transfer rates, and pressure distributions are sensitive to upstream thermodynamic flow conditions, shock strength, and Mach number.[1,2,8,9] In addition, experimental[2,10] and computational[3–5,9,11] work indicates that the type IV interaction is unsteady. In particular, for the chosen geometries, interaction frequencies on the order of 1–32 kHz were found.

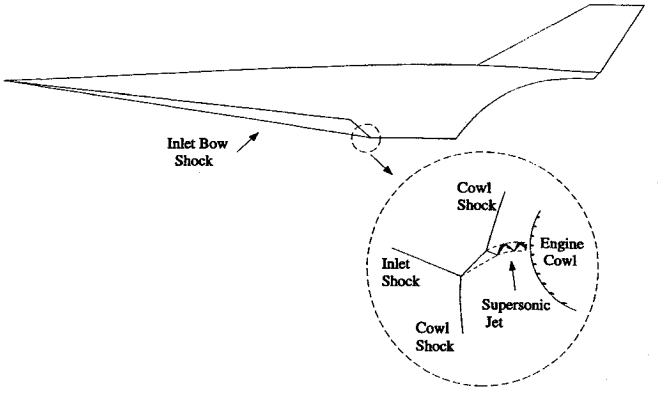

Fig. 1 Generic hypersonic vehicle showing the type IV shock interaction.

Presented as Paper 93-2479 at the AIAA/SAE/ASME/ASEE 29th Joint Propulsion Conference, Monterey, CA, June 28–30, 1993; received Jan. 5, 1994; revision received April 1, 1995; accepted for publication April 16, 1995.

*Graduate Research Assistant, Department of Aerospace Engineering; currently ONR Postdoctoral Fellow, Department of Aerospace Engineering, U.S. Naval Academy, Annapolis, MD 21402. Member AIAA.

†Associate Professor, Department of Aerospace Engineering. Senior Member AIAA.

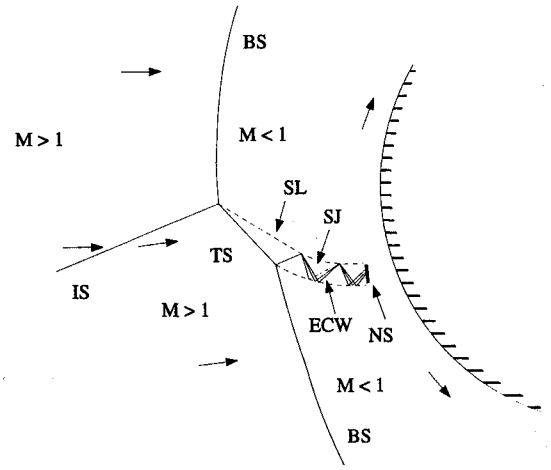

Fig. 2 Type IV shock interaction. BS, bow shock; ECW, expansion/compression waves; IS, impinging shock; NS, normal shock; SL, shear layer; SJ, supersonic jet; and TS, transmitted shock.

Until recently, relatively little work has been done to explain this unsteadiness or the mechanism that drives it. Previous work has suggested the following possible causes for this unsteadiness: 1) shear-layer turbulence, 2) turbulent interactions at the jet impingement location, 3) acoustic feedback within the subsonic region, and 4) sensitivity of the interaction to upstream variations.

Analytical work has shown that variations in the upstream conditions will not have a significant effect on the unsteadiness of the type IV shock interaction at high hypersonic speeds.[12] However, at moderate hypersonic speeds upstream unsteadiness may affect the shock unsteadiness. Therefore, if the type IV interaction is unsteady, then it would most likely be associated with the physics of the type IV shock interaction and not with variations in upstream conditions.

This work first considers the effect of different impinging shock strengths and impinging shock locations on the type IV shock interaction. The time evolution of the supersonic jet is then presented. Finally, a detailed flowfield analysis is numerically presented from which the mechanism of the unsteadiness is discussed.

Numerical Algorithm

In the present work the TIMETVD code of Yee,[13] which solves the two-dimensional Navier–Stokes equations in generalized curvilinear coordinates, is used. The total variation diminishing (TVD) scheme utilized in this work is described by Yee and assumes laminar flow and a perfect gas. Roe's averaging is used to describe the inviscid components of the flux, as described by Yee. The Euler implicit method is used for the time integration and the explicit viscous terms are centrally differenced.

Code validation for this version of the TIMETVD algorithm has been performed by Lind[6] and Lee.[14]

Initial and Boundary Conditions

A blunt body solution is first calculated on each of the grids used in this study. This converged solution was used as the initial condition. At $t = 0$, an impinging shock is introduced into the flowfield. A no-slip velocity condition, constant temperature, and zero pressure gradient are all assumed at the body surface. A first-order approximation to the pressure gradient was applied.

The outflow boundary, which is supersonic for all calculations, is extrapolated from the adjacent grid point. For the blunt-body solution freestream values are used for all points on the inflow boundary. For the shock-interaction cases freestream conditions are assigned to the points on the inflow boundary above the shock impingement point and values given by the Rankine–Hugoniot equation for the given freestream Mach number and shock strength are assigned to the remaining inflow points. A schematic diagram of the initial and boundary conditions is shown in Fig. 3.

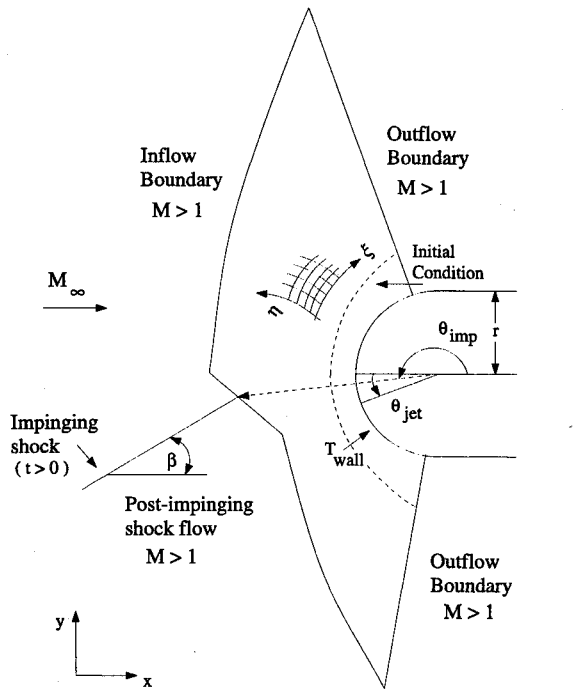

Fig. 3 Schematic diagram of computational and physical domain and initial and boundary conditions.

Grid Generation

To provide smooth variation of the grid points throughout the physical domain, grid clustering in regions of high gradients and grid orthogonality, a two-step grid-generation process was utilized. An algebraic grid was generated and used as input to an elliptic grid solver. The algebraic grid algorithm allowed for the generation of the body, outside boundary, and clustering of grid points circumferentially in regions of interest. In particular, the points on the outside boundary were clustered near the impinging shock location and points on the solid boundary were clustered near the impingement region of the supersonic jet. The elliptic solver was used to ensure smoothness of the grid, orthogonality of the grid lines at the solid surface, and grid clustering at the solid boundary.

Table 1 summarizes the grids used in this study. In this table SIA is the shock impingement angle or the angle at which the shock intersects the inflow boundary, as shown in Fig. 3. $\Delta\theta_{\text{grid}}$ is the angular difference between two adjacent grid points at the shock impingement location on the outside grid and is an indication of the circumferential grid resolution at the shock impingement region. $\Delta\theta_{\text{body}}$ is defined in the same way as $\Delta\theta_{\text{grid}}$, but at the jet impingement location. $(x, y)_{\text{grid}}$ is the location of the impinging shock on the inflow grid. θ_{orth} gives the average grid orthogonality at the body near the jet impingement location. In addition, the circular cylinder was centered at the origin, the normal distance from the body to the first grid point was 3.38×10^{-5} m, and the cell Reynolds number at the body, $Re_c = \rho_\infty a_\infty \Delta y_{\text{body}}/\mu_\infty$, was 4.21×10^2.

Algebraic Grid Generation

The solid body was modeled as a circular cylinder. The freestream boundary was generated using the shock correlations of Billig.[15] Since Billig's correlations give the exact shock shape, multiplicative factors of this equation were used

Table 1 Summary of grids used in this study

Grid no.	Grid size	β, deg	SIA, deg	$\Delta\theta_{grid}$, deg	$\Delta\theta_{body}$, deg	$(x, y)_{grid}$, m	θ_{orth}, body, deg
1	88 × 88[a]	18.0	177.80	0.60	0.55	(−0.358, −1.37E-2)	89.8
2	121 × 121	19.0	184.19	0.30	0.49	(−9.75E-2, −7.13E-3)	89.6
3	181 × 160	19.0	185.08	0.34	0.22	(−9.54E-2, −8.47E-3)	89.7

[a]Representative grid.

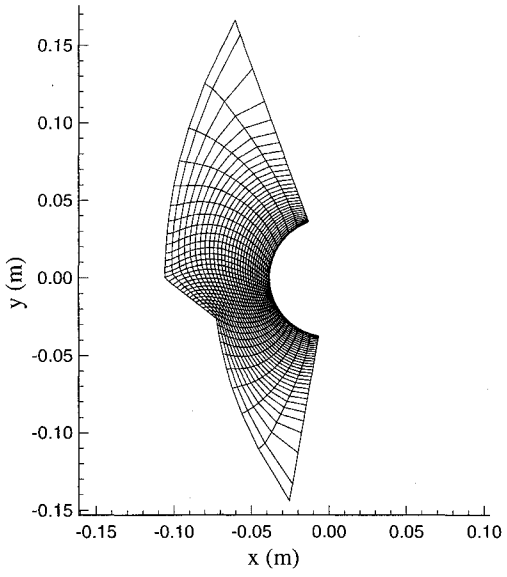

Fig. 4 Typical 181 × 160 semiadaptive elliptic grid. (Note: For clarity, every third point in the ξ and η direction is shown.)

to generate the upper and lower segments of the outside boundary so as to conform to the geometry of the type IV interaction. These segments were connected by a straight line.

Clustering in the circumferential direction was performed separately on the solid and outside boundary and was accomplished by using the following stretching function from Hoffmann[16]:

$$x = \xi, \qquad y = D\left\{1 + \frac{\sinh[B(\eta - A)]}{\sinh(BA)}\right\} \tag{1}$$

where A is given by

$$A = \frac{1}{2B} \ln \frac{1 + (e^{B} - 1)(D/H)}{1 + (e^{-B} - 1)(D/H)} \tag{2}$$

In Eqs. (1) and (2), B controls the amount of clustering, H is the total length of the direction being considered, D is the y coordinate where clustering is desired, and ξ and η are the coordinates in the computational space.

Elliptic Grid Generation

To ensure orthogonality at the solid surface and to smooth the grid the elliptic grid generation algorithm developed by Sorenson[17] was used. In addition to grid orthogonality the algorithm allows the user to specify the spacing between the solid body and the grid point immediately above it. A typical grid used in this study is shown in Fig. 4.

Baseline Test Case

In this study the experimental work of Holden,[18] in particular run 24 of that study, is used as a baseline for Mach number, Reynolds number, and overall geometry. This data is summarized in Table 2 along with the assumptions for the present computational work. In this table, Δx is the distance from the edge of the plate to the front of the cylinder and Δy is the distance from the center of the cylinder to the top of the wedge generator. The shock angle β_{calc} was determined from the given wedge angle and freestream Mach number. β_1 and β_2 are the two shock angles used in this work. β_1 was chosen to be representative of the shock angle given by the freestream Mach number and shock deflection angle in inviscid flow, and β_2 approximates the shock angle measured directly from the photograph for run 24 of Holden. No attempt was made to find the location of the impinging shock that resulted in the correct distribution of pressure along the cylinder surface for run 24; hence, no comparisons with the experimental results will be performed.

Table 2 Experimental conditions for run 24 and computational assumptions

Experimental conditions of run 24	Computational assumptions
Wedge length, 0.6731 m	γ, 1.4
Wedge angle, 12.50 deg	T_{wall}, 954K
Δx, 1.50E-0.2 m	β_1, 18.0 deg
Δy, 7.34E02	β_2, 19.0 deg
M_∞, 8.144	
Re/m, 1.243 × 10^7	
H_{wall}, 2.957 × 10^5 (m/s)^2	
β_{calc}, 18.04 deg	

Results

It has been suggested by Hoffmann[19] and Klopfer and Yee[3] that the calculation of heat transfer is a function of the distance from the body to the first grid point $\Delta\eta$. However, the pressure is not as sensitive to this distance and a grid spacing that is several orders of magnitude greater is sufficient to accurately predict the pressure. To accurately predict the heat transfer in this work it is estimated that this distance would have to be at least 10^{-7} m. Since grid spacing of this order would drastically and unrealistically increase the computational effort required and since this work is directed more towards the unsteady phenomena, which pressure measurements can accurately analyze, heat transfer results were not calculated.

Parametric Studies

The sensitivity of peak pressure and jet impingement location to the shock impingement angle and shock strength is shown in Fig. 5. This study was performed on the 88 × 88 grid. Impinging shock angles of 18 and 19 deg were considered and the location of the impinging shock on the outer boundary varied from $177.80 \leq \theta \leq 187.97$ deg. In this figure, the nonlinear variation of peak pressure and jet impingement angle with the shock impingement angle is shown. Also notice in this figure that a change in shock angle, from 18 to 19 deg, for a shock impingement angle of 182.44 deg, results in a peak pressure increase of 21% and a 4-deg change in the jet impingement angle. For the 19-deg shock angle calculation notice that a 3-deg change in the shock impingement angle re-

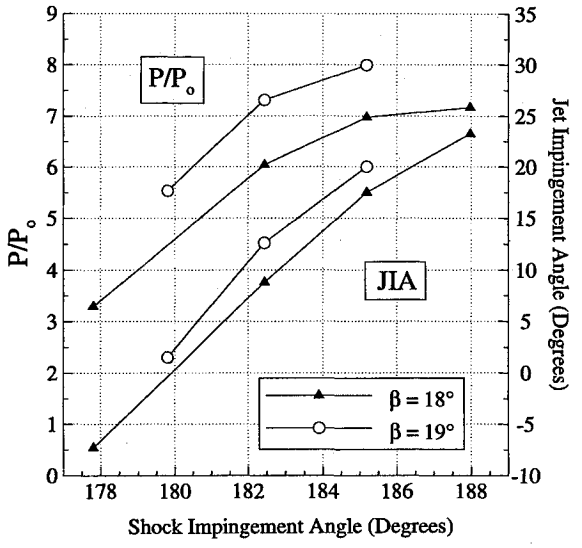

Fig. 5 Effect of shock strength and shock impingement angle on jet impingement angle and peak pressure.

sults in an angular change of 11 deg in the jet impingement location and a 32% change in the peak surface pressure. This is an indication of the sensitivity of the impinging shock location on the interaction.

Jet Unsteadiness

Under certain conditions the previous analysis yielded an unsteady supersonic jet, as can be seen in a plot of the time history of the peak pressure. The effect that a change in shock impingement angle θ and shock strength, given by a shock angle of β, have on the time variation of peak surface pressure and its position is shown in Fig. 6. These cases were also studied on the 88 × 88 grid. In these figures the discrete variation in the jet impingement angle with time is due to the limits of grid resolution at these points.

Figure 6a shows the time variation of peak pressure and its location for β = 18 deg and for θ = 182.44 and 185.19 deg. Notice that for these shock impingement angles the flowfield reaches a steady state in approximately 35 and 45 ms, respectively.

When β is increased to 19 deg, an increase of just 1 deg, the interaction does not reach steady state at shock impingement angles of 179.77 deg or for 185.19 deg within the 60-ms run time, as shown in Fig. 6b. The resulting flowfield appears to approach a quasisteady state, in that all of the initial transients have subsided and the supersonic jet has evolved into a damped, oscillatory motion.

Considering the 185.19-deg shock impingement angle and 18- and 19-deg shock angles, given by the hollow symbols in Fig. 6, notice that the result of the stronger shock is that the interaction is not damped as quickly. That is, the amplitude of the peak pressure and jet impingement angle becomes larger and the unsteady phenomena do not damp out as quickly, as indicated by the fact that the steady state has not been reached in the 60-ms run time.

Although the time history of peak pressure and jet impingement angle is damped in time, for this course 88 × 88, high-frequency oscillations are still apparent. In particular, a high-frequency oscillation on the order of 1.4 kHz is modulating a lower frequency response.

The development of the supersonic jet, as shown by time progression of surface pressure, is shown in Fig. 7 for a 185.19-deg shock impingement point and shock angles of 18 and 19 deg. For both shock angles the transformation of the flowfield from the blunt body solution to the type V then back to the type IV is clearly seen. In particular, note that for a shock

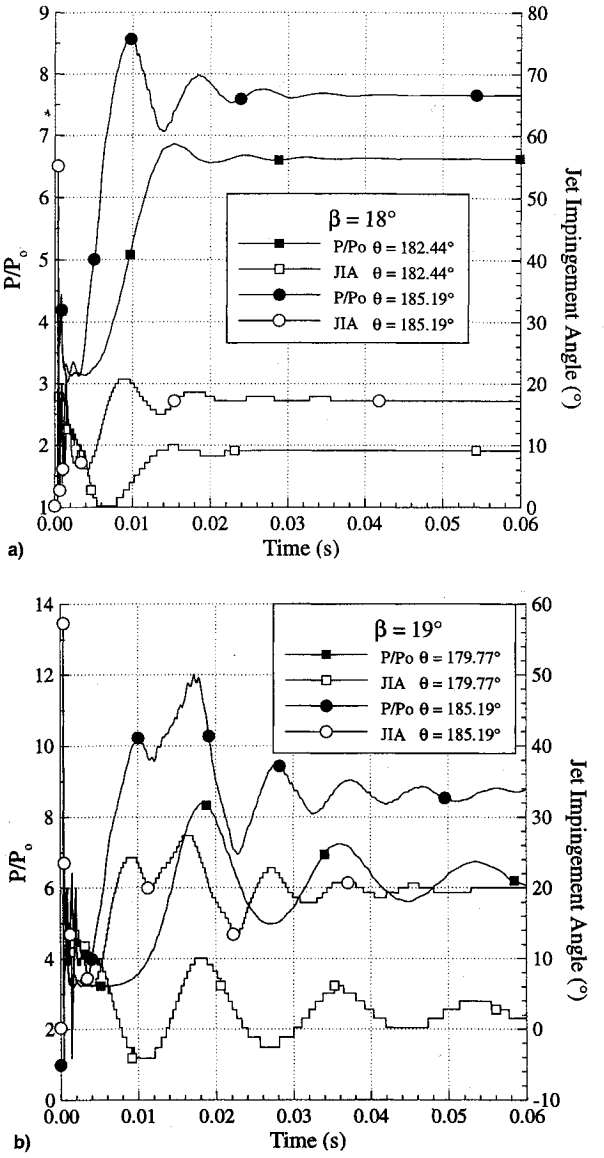

Fig. 6 Time history of peak pressure and jet impingement angle for various shock impingement angles. β = a) 18 and b) 19 deg.

angle of 18 deg, shown in Fig. 6a, the surface pressure reaches a steady-state solution. However, for an impinging shock angle of 19 deg, shown in Fig. 6b, the surface pressure distribution does not reach steady state within the 60-ms run.

To study this interaction in more spatial detail the grid density was increased to a 181 × 160 grid. A time history of the peak pressure and as well as the position of this peak pressure is shown in Fig. 8 for a shock impingement angle of 187.08 deg. The oscillatory behavior of the jet is clearly shown. As depicted in Fig. 8b, the frequency of oscillation is measured to be 1.38 kHz. A Fourier analysis of the quasisteady flowfield was performed for this solution, as well as a solution conducted on a 121 × 121 grid. The analysis on the more dense grid resulted in a high-frequency oscillation of 1.39 kHz superimposed on a 85-Hz carrier signal. The solution on the 121 × 121 grid had a 1.45-kHz signal riding on a 100-Hz signal.

Figure 8 shows that the higher frequency oscillation, associated with the rapid back and forth jet motion, is superimposed on the lower frequency oscillation. The mechanism driving the lower frequency oscillation is the transient response to imposition of initial conditions. The Strouhal number based on cylinder diameter St_d is approximately 5.6 × 10^2 for the higher frequency oscillation. Future parametric

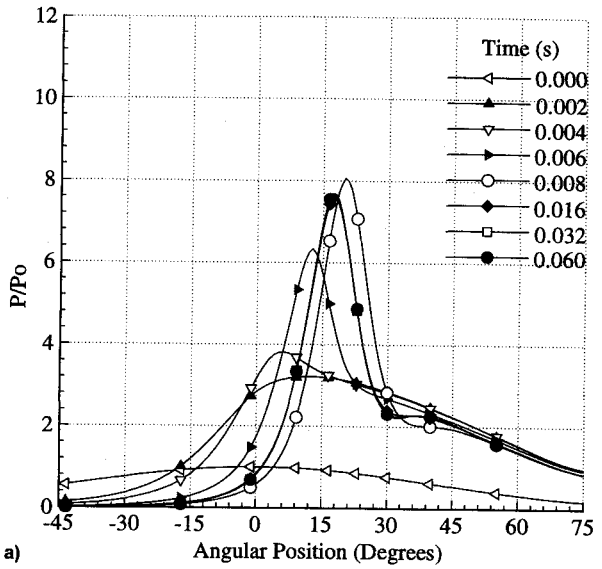

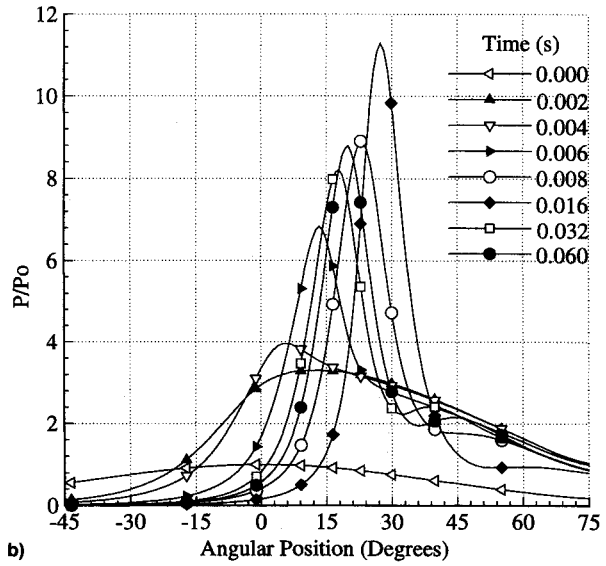

Fig. 7 Surface pressure at various time steps for shock impingement angle of 185.19 deg. β = a) 18 and b) 19 deg.

work will be performed to determine if there is a correlation between Strouhal number and the other similarity parameters.

Detailed Flowfield Analysis

A spatially detailed flowfield calculation was performed on the 181 × 160 grid. A 19-deg impinging shock was chosen with a shock impingement location of 185.077 deg. For these calculations a time increment of 10^{-3} ms was chosen, which resulted in a maximum Courant–Friedrichs–Lewy number of 0.9995.

Plots of the streamline patterns as well as vorticity contours, as discussed in Lind,[6] lead to the conclusion that the resulting unsteady flow is related to the formation and shedding of a strong vortex, production of which is due to the high-velocity gradient across the shear layer that bounds the upper part of the supersonic jet. When the vortex reaches a minimum pressure, it breaks down, resulting in the shedding of shear layers and formation of embedded shocks that propagate over the cylinder. A schematic diagram of these flow features is shown in Fig. 9.

Figure 10 shows schematically the evolution of the flowfield over one time cycle of peak pressure. Figures 11a–11d show

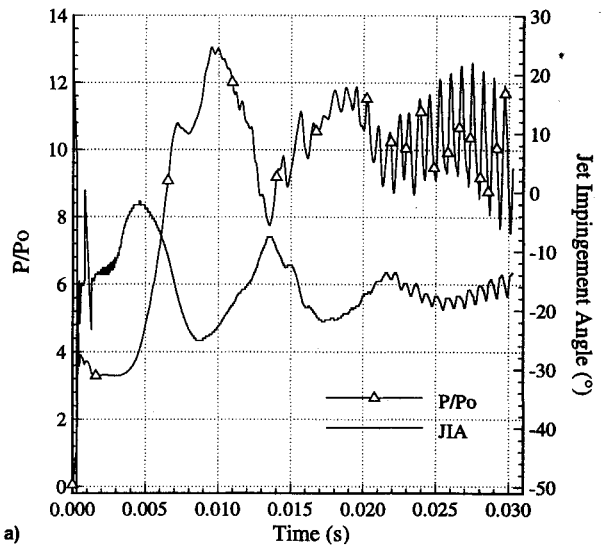

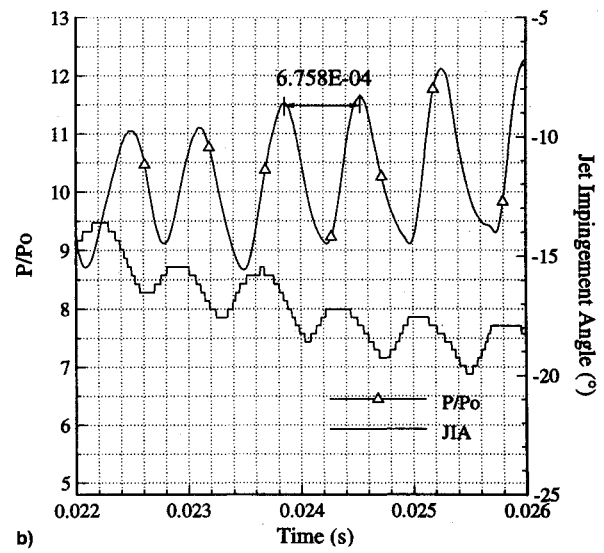

Fig. 8 Time variation of peak pressure and jet impingement point for 181 × 160 grid and a shock impingement angle of 185.08 deg.

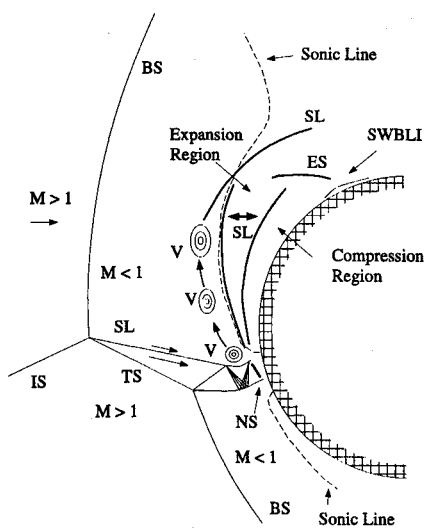

Fig. 9 Schematic diagram of the computed flowfield. BS, bow shock; ECW, expansion/compression waves; ES, embedded shock; IS, impinging shock; NS, normal shock; SL, shear layer; SJ, supersonic jet; SWBLI, shock wave/boundary-layer interaction; TS, transmitted shock; and V, vortex.

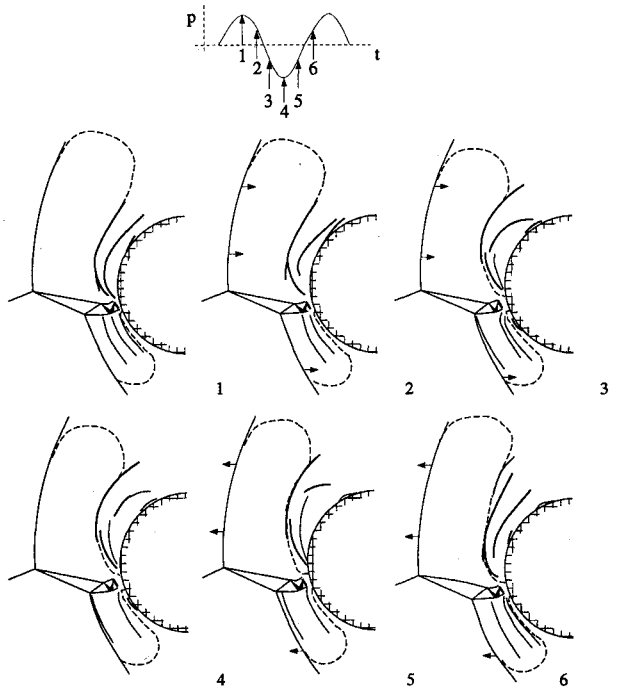

Fig. 10 Schematic diagram of the time evolution of flowfield.

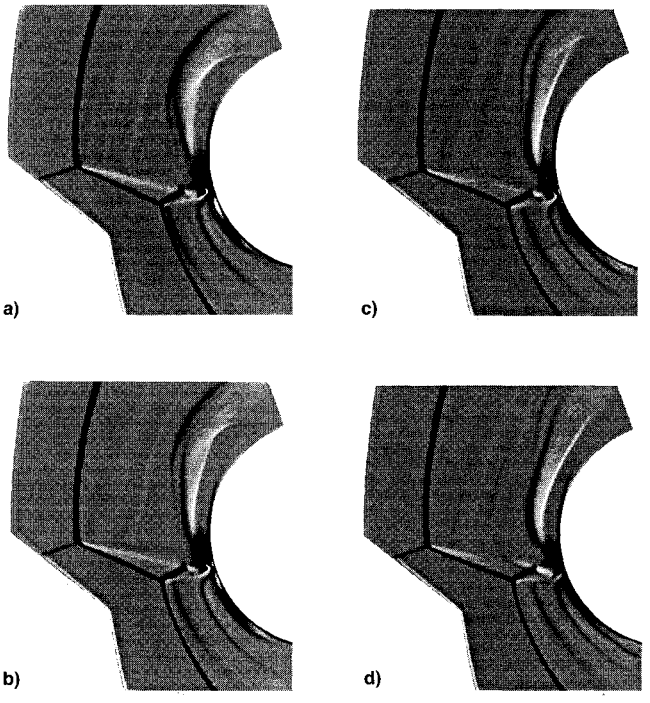

Fig. 11 Schlieren type plot of flowfield over one-half time cycle. t = a) 23.50, b) 23.60, c) 23.70, and d) 23.80 ms.

computationally generated schlieren diagrams for the latter half of this cycle, $23.50 \leq t \leq 23.80$ ms, at 0.1-ms increments. Schlieren-type plots are gradients of density in the x direction, and hence, the dark regions indicate an increase in density, whereas the light regions show a decrease in density. The density contour levels are arbitrarily chosen to show specific flow features. Comparing these figures with the time variation of pressure and jet impingement angle shown in Fig. 8, it is seen that $t = 23.50$ ms corresponds to the time when peak pressure is at a minimum. The remaining plots are presented at 0.1-ms increments for just over one-half cycle of oscillation.

The phenomena exhibited in Figs. 10 and 11 may be best explained if one analyzes half a pressure cycle at a time. Consider first the cycle depicted by points 1–4 in Fig. 10. At point 1, the upper and lower shocks are farthest away from the body. Because of the large velocity gradient across the shear layer, which extends from the upper shock and forms the upper portion of the supersonic jet, a vortex forms near the junction where the supersonic jet impinges the body. As this vortex increases in strength, decreasing the local pressure, the outer shock structure moves towards the body and the jet moves upward. At the same time the end portion of the expansion region, which is bounded by shear layers, bends towards the body.

As the expansion region continues to bend the lower trailing portion of the shear layer forms into a shock, which then interacts with the boundary layer, resulting in a mild separated region. At this point in time, the shock wave detaches from the shear layer and propagates downstream, degenerating with time. At about the same instant in time the pressure associated with the vortex reaches a minimum. This is point 4 in Fig. 10.

At later times, $23.50 < t < 23.90$ ms, shown in Figs. 11a–11d, the vortex weakens, increasing the local pressure, and the shock structure moves out. Consider once again Fig. 8b along with the computational schlieren plots of Fig. 11. Notice that the variation of the jet impingement angle remains constant over a very short time period after the peak pressure has reached a local minimum. It is at this time that the vortex is strongest.

In addition to the shock motion and the generation of vorticity, the schlieren-type plots also show the generation and shedding of shear layers. By following the shear layer in time one finds that the frequency of shedding is approximately 1.4 kHz. This is the same frequency found by direct measurement of the time variation of pressure as well as by the Fourier analysis performed on the time history of the peak pressure.

Conclusions

The unsteady characteristics of the type IV shock interaction have been numerically investigated using the thin-layer formulation of the Navier–Stokes equations coupled with a high-resolution, implicit TVD scheme.

The high-frequency jet unsteadiness is seen to be related to the formation of a vortex near the junction of upper shear layer and the termination point of the supersonic jet, its breakdown, and then its propagation along the upper portion of the cylinder, causing shear layers to be generated and then shed.

The jet unsteadiness is also a function of the shock strength and its impingement angle. The oscillatory motion of the peak pressure is strongly dependent on the shock strength. Small deviations in the impinging shock properties can drive a steady-state flowfield to an unsteady one.

The computational work presented here did not include turbulence modeling. The effect of turbulence, especially in regions near the shear layer and the jet impingement point may influence the frequency and magnitude of the unsteadiness; this will be included in future work.

Acknowledgments

This work was conducted under the support of NASA Langley Research Center, with Ajay Kumar as Technical Monitor, NASA Grant NAG-11333-S1. The authors would like to thank Helen Yee at the NASA Ames Research Center for introducing us to the importance of this work and for the use of her TIMETVD code. The authors would also like to thank D. J. Singh for helpful discussions, Ashish Nedungadi for reviewing the original manuscript, and Jang Lee for his invaluable assistance with the code and reviewing the original manuscript. Appreciation is also expressed to the JPL Supercomputing Center and the San Diego Supercomputing Center for their generous computing time.

References

[1]Edney, B., "Anomalous Heat Transfer and Pressure Distributions on Blunt Bodies at Hypersonic Speeds in the Presence of an Impinging Shock," Aeronautical Research Inst. of Sweden, FAA Rept. 115, Feb. 1968.

[2]Holden, M. S., Wieting, A. R., Moselle, J. R., and Glass, C., "Studies of Aerothermal Loads Generated in Regions of Shock/Shock Interaction in Hypersonic Flow," AIAA Paper 88-0477, Jan. 1988.

[3]Klopfer, G. H., Yee, H. C., and Kutler, P., "Numerical Study of Unsteady Viscous Hypersonic Blunt Body Flows with an Impinging Shock," NASA TM 100096, April 1988.

[4]Prabhu, R. K., Stewart, J. R., and Thareja, R. R., "Shock Interference Studies on a Circular Cylinder at Mach 16," AIAA Paper 90-0606, Jan. 1990.

[5]Gaitonde, D., and Shang, J. S., "The Performance of Flux-Split Algorithms in High-Speed Viscous Flows," AIAA Paper 92-0186, Jan. 1992.

[6]Lind, C. A., "A Computational Analysis of the Unsteady Phenomena Associated with a Hypersonic Type IV Shock Interaction," Ph.D. Dissertation, Dept. of Aerospace Engineering, Univ. of Maryland, College Park, MD, 1994.

[7]Francis, W. L., "Experimental Heat-Transfer Study of Shock Impingement on Fins in Hypersonic Flow," *Journal of Spacecraft and Rockets*, Vol. 2, July 1965, pp. 630–632.

[8]Keyes, J. W., and Hains, F. D., "Analytical and Experimental Studies of Shock Interference Heating in Hypersonic Flow," NASA TN D-7139, May 1973.

[9]Lind, C. A., and Lewis, M. J., "A Numerical Study of the Unsteady Processes Associated with the Type IV Shock Interaction," AIAA Paper 93-2479, June 1993.

[10]Nowak, R., Holden, M. S., and Wieting, A. R., "Shock/Shock Interference on a Transpiration Cooled Hemispherical Model," AIAA Paper 90-1643, June 1990.

[11]Singh, D. J., Kumar, A., and Tiwari, S. N., "Numerical Simulation of Shock Impingement on Blunt Cowl Lip in Viscous Hypersonic Flows," *Numerical Heat Transfer, Part A*, Vol. 20, No. 3, 1991, pp. 329–344.

[12]Lind, C. A., and Lewis, M. J., "Sensitivity of Shock-Shock Interactions to Upstream Variations," *Journal of Propulsion and Power*, Vol. 7, No. 6, 1991, pp. 1074–1076.

[13]Yee, H. C., and Harten, A., "Implicit TVD Schemes for Hyperbolic Conservation Laws in Curvilinear Coordinates," *AIAA Journal*, Vol. 25, No. 2, 1987, pp. 266–274.

[14]Lee, J. Y., "A Numerical Study of the Flow Establishment Time in Hypersonic Shock Tunnels," M.S. Thesis, Univ. of Maryland, Rept. UM-AERO 91-04, College Park, MD, 1991.

[15]Billig, F. S., "Shock-Wave Shapes Around Spherical- and Cylindrical-Nosed Bodies," *Journal of Spacecraft and Rockets*, Vol. 4, No. 6, 1967, pp. 822, 823.

[16]Hoffmann, K. A., *Computational Fluid Dynamics for Engineers*, Engineering Education System, Austin, TX, 1989.

[17]Sorenson, R. L., "A Computer Program to Generate Two-Dimensional Grids About Airfoils and Other Shapes by the Use of Poisson's Equation," NASA TM 81198, May 1980.

[18]Holden, M. S., Moselle, J. R., Lee, J., Wieting, A. R., and Glass, C., "Studies of Aerothermal Loads Generated in Regions of Shock/Shock Interaction in Hypersonic Flow," Calspan-UB Research Center, NAS1-17721, Oct. 1991.

[19]Hoffmann, K. A., Siddiqui, M. S., and Rutledge, W. H., "Effect of the Grid System on Heat Transfer Computations for High Speed Flows," *Numerical Grid Generation in Computational Fluid Dynamics and Related Fields*, Elsevier, Amsterdam, 1991.